

Application of Renyi Entropy to Detect Subtle Changes in Scattering Architecture

M.S. Hughes¹, J.E. McCarthy², J.N. Marsh¹, J.M. Arbeit¹, R.G. Neumann¹, R.W. Fuhrhop¹, K.D. Wallace¹, T. Thomas¹, J. Smith¹, K. Agyem¹, G. M. Lanza¹, and S. A. Wickline¹

¹Washington University School of Medicine

²Department of Mathematics, Washington University

(Dated: August 26, 2008)

Previously we reported on an entropy-based signal receiver and demonstrated that, in certain settings, it was more sensitive to subtle changes in scattering architecture than conventional energy-based signal characterization¹. In this paper we present results demonstrating further improvements in sensitivity using a signal receiver based on the Renyi-entropy.

I. INTRODUCTION

In an earlier paper we reported on the comparison between a Shannon Entropy analog, H_f , and more conventional signal processing techniques, *i.e.*, signal energy and its logarithm as applied to beam formed radiofrequency (RF) data. Both analysis techniques were applied to data obtained in backscatter measurements from nanoparticle targeted neovasculature¹. The comparison study was undertaken after a preliminary conventional B-mode grayscale analysis of the data was unable to detect changes in backscattered RF arising from the accumulation of targeted nanoparticles in the neovasculature in the insonified region. This result implied that acoustic characterization of sparse collections of targeted perfluorocarbon nanoparticles presented challenges that might require the application of novel types of signal processing. We were able to show that signal processing based on a “moving window” H_f analysis could distinguish the difference in backscatter measured at 15 and 60 minutes and (although it was not stressed) able to detect accumulation of targeted nanoparticles 30 minutes post-injection. The signal energy, defined as the sum of squares of the signal amplitude over the same moving window, was unable to distinguish measurements made at any time during the one hour experiment.

We stress that, although entropy-based techniques have a long history for image enhancement and post processing of reconstructed images, the approach we have taken is different in that entropy is used directly as the quantity defining the pixel values in the image. Specifically, images are reconstructed by computing H_f for segments of the individual RF A-lines that comprise a typical medical image by applying a “moving window”, or “box-car”, analysis. The local computation of an entropy value for each location within an image is therefore possible.

II. APPROACH

All RF data are obtained by sampling a continuous function, $y = f(t)$, and subsequently using the sampled values to compute its associated density function, $w_f(y)$.

A. The function $w_f(y)$

The density function $w_f(y)$ may be used to compute the entropy H_f . It corresponds to the density functions used in statistical signal processing. From it, other mathematical quantities are subsequently derived (*e.g.*, mean values, variances, covariances)²⁻⁴. While the density function is usually assumed to be continuous, infinitely differentiable, and to approach zero at infinity in statistical signal processing of random signals, in our application $w_f(y)$ has (integrable) singularities.

As in previous studies, we employ the convention that the domain of $f(t)$ is $[0, 1]$, so that, $w_f(y)$, the density function of $f(t)$, can be defined by the basic integral relation

$$\int_0^1 \phi(f(t)) dt = \int_{f_{min}}^{f_{max}} \phi(y)w_f(y)dy, \quad (1)$$

Equation (1) implies

$$w_f(\xi) = \sum_{\{t_k|f(t_k)=\xi\}} \frac{1}{|f'(t_k)|}, \quad (2)$$

either by breaking the integral into a sum over intervals of monotonicity of $f(t)$ (“laps”) and changing variables, or by choosing $\phi(y)$ to be a Dirac delta function and using the well-known expansion formula for a delta function of a function⁵. We will assume that all digitizable waveforms $f(t)$ are comprised of at least one section, or “lap”, where it is monotonic. The lap boundaries are just the points t where $f'(t) = 0$. On each lap, $f(t)$ has a well-defined inverse function. These may be used to rewrite Eq. (2)

$$w_f(y) = \sum_{k=1}^N |g'_k(y)|, \quad (3)$$

where N is the number of laps, $g_k(y)$ is the inverse of $f(t)$ in the k^{th} -lap and if y is not in the range of $f(t)$ in the k^{th} -lap, $g'_k(y)$ is taken to be 0.

For experimentally measured data, we may also assume that all digitizable waveforms $f(t)$ have a Taylor series

expansion at all points in $[0, 1]$. Then near a time t_k such that $f'(t_k) = 0$

$$y = f(t) = f(t_k) + \frac{1}{2!} f''(t_k) (t - t_k)^2 + \dots, \quad (4)$$

t_k is a lap boundary and on the left side of this point Eq. (4) may be truncated to second order and inverted to obtain

$$g_k(y) \sim t_k \pm \sqrt{2(y - f(t_k))/f''(t_k)}, \quad (5)$$

with

$$|g'_k(y)| \sim 1/\sqrt{2f''(t_k)(y - f(t_k))}. \quad (6)$$

The contribution to $w_f(y)$ from the right side of the lap boundary, from $g_{k+1}(y)$, is the same, so that the overall contribution to $w_f(y)$ coming from the time interval around t_k is

$$|g'_k(y)| \sim \sqrt{2/(f''(t_k)(y - f(t_k)))}, \quad (7)$$

for $0 < f(t_k) - y \ll 1$ for a maxima at $f(t_k)$ and $0 < y - f(t_k) \ll 1$ for a minima. Thus, $w_f(y)$ has only a square root singularity (we have assumed that t_k is interior to the interval $[0, 1]$; if not, then the contributions to w_f come from only the left or the right). If additionally, $f''(t_k) = 0$ then the square root singularity in Eq. (6) will become a cube-root singularity, and so on, so that the density functions we consider will have only integrable algebraic singularities.

Figure (1) illustrates, schematically, one possible type of behavior possible in $w_f(y)$: both discontinuities and algebraic singularities (indicated by arrows on the plots of $w_f(y)$). Progressing from left to right in the figure illustrates how to estimate qualitative features of $w_f(y)$ from $f(t)$. For instance, the maxima in $f(t)$ correspond to an algebraic singularities in $w_f(y)$, plotted sideways in the middle panel to more clearly indicate the relationship between its features and those of $f(t)$. The rightmost panel shows $w_f(y)$ in a conventional layout (a rotated and flipped version of the plot in the middle panel). These plots show that the density functions possess significantly different attributes from those usually considered in statistical signal processing.

The mathematical characteristics of the singularities are important in order to guarantee the existence of the following integral on which we base our analysis of signals in this study:

$$I_f(r) = \frac{1}{1-r} \log \left[\int_{f_{min}}^{f_{max}} w_f(y)^r dy \right], \quad (8)$$

which known as the Renyi entropy⁶. The physical significance of the parameter r appearing in Eq. (8) may be interpreted by analogy with statistical mechanics where the probabilities $w_f(y)$ are given in terms of system energy levels according to

$$E(y) = \frac{1}{\mu_0} \log[w_f(y)], \quad (9)$$

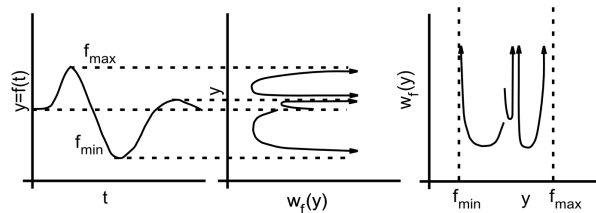


FIG. 1. A time-domain waveform, $f(t)$ with three critical points(left), and its associated density function $w_f(y)$ has three corresponding (integrable) singularities.

(with μ_0 being a physical constant) and thermodynamic quantities are derived from the partition function,

$$Z = \int e^{-\mu E(y)} dy = \int w_f(y)^{\frac{-\mu}{\mu_0}} dy, \quad (10)$$

where $\mu = 1/(kT)$, with k being Boltzman's constant and T being temperature⁷. From the equations we see that the Renyi entropy, $I_f(r)$ is very similar to the partition function in statistical mechanics and that the parameter r is analogous to an inverse "temperature" Moreover, $I_f(r) \rightarrow -H_f$, as $r \rightarrow 2$, using L'Hopital's rule, so that I_f is a generalization of H_f :

$$H_f = \int_{f_{min}}^{f_{max}} w_f(y) \log w_f(y) dy, \quad (11)$$

which previous studies have shown can be more sensitive to subtle changes in scattering architecture than are more commonly used energy-based measures.¹ The purpose of this study is to show that further sensitivity improvements may be obtained using I_f at the suitable value of r .

For the density functions $w_f(y)$ encountered in our study, $I_f(r)$ is undefined for $r \geq 2$. Moreover, as $r \rightarrow 2^-$, the integral appearing in Eq. (8) will grow without bound due to the singularities in the density function, $w_f(y)$ (i.e., Eq. (7)). The behavior as $r \rightarrow 2$ is dominated by contributions from the singularities. If the k^{th} critical point is a minima (the argument for a maxima is similar) the contribution to the integral in Eq. (8) is asymptotic to

$$\lim_{\epsilon \rightarrow 0} \int_{f(t_k)}^{f_{max}} \left(\frac{a_k}{\sqrt{y - f(t_k)}} \right)^{2-\epsilon} dy. \quad (12)$$

This is equal to

$$\begin{aligned}
&= \lim_{\epsilon \rightarrow 0} a_k^{2-\epsilon} \int_{f(t_k)}^{f_{max}} (y - f(t_k))^{1-\epsilon/2} dy, \\
&= \lim_{\epsilon \rightarrow 0} a_k^{2-\epsilon} \frac{(y - f(t_k))^{\epsilon/2}}{\epsilon/2} \Big|_{f(t_k)}^{f_{max}}, \\
&= \lim_{\epsilon \rightarrow 0} a_k^{2-\epsilon} \frac{(f_{max} - f(t_k))^{\epsilon/2}}{\epsilon/2}, \\
&= \lim_{\epsilon \rightarrow 0} \frac{2a_k^2}{\epsilon}, \tag{13}
\end{aligned}$$

where $a_k = \sqrt{2/f''(t_k)}$. [Aside: for a maxima we have the asymptotic term

$$\lim_{\epsilon \rightarrow 0} \int_{f_{min}}^{f(t_k)} \left(\frac{a_k}{\sqrt{f(t_k) - y}} \right)^{2-\epsilon} dy. \tag{14}$$

This is equal to

$$\begin{aligned}
&= \lim_{\epsilon \rightarrow 0} a_k^{2-\epsilon} \int_{f_{min}}^{f(t_k)} (f(t_k) - y)^{1-\epsilon/2} dy, \\
&= \lim_{\epsilon \rightarrow 0} a_k^{2-\epsilon} \frac{(f(t_k) - y)^{\epsilon/2}}{\epsilon/2} \Big|_{f_{min}}^{f(t_k)}, \\
&= \lim_{\epsilon \rightarrow 0} a_k^{2-\epsilon} \frac{(f(t_k) - f_{min})^{\epsilon/2}}{\epsilon/2}, \\
&= \lim_{\epsilon \rightarrow 0} \frac{2a_k^2}{\epsilon}, \tag{15}
\end{aligned}$$

where now have a different expression for $a_k = \sqrt{-2/f''(t_k)}$.]

This behavior is shown in the left panel of Figure (2). Moreover, as shown in the right panel it is possible that two slightly different functions, $f(t)$ and $f(t)+\xi(t)$, where ξ is small, may have entropies, H_f and $H_{f+\xi}$ that are close, as shown in the figure, but whose Renyi entropies, $I_f(r)$ and $I_{f+\xi}(r)$ diverge as $r \rightarrow 2$. If this amplification effect were not dominated by noise, it would permit separation of subtly different functions, such as those obtained from measurements of backscattered ultrasound of targeted and nontargeted tissue. Our results show that this can happen in practice.

III. MATERIALS AND METHODS

A. Nanoparticles for molecular imaging

A cross-section of the spherical liquid nanoparticles used in our study is diagrammed in Figure (3). For *in vivo* imaging we formulated nanoparticles targeted to $\alpha_v\beta_3$ -integrins of neovascularity in cancer by incorporating an ‘‘Arg-Gly-Asp’’ mimetic binding ligand into the lipid layer. Methods developed in our laboratories were used to prepare perfluorocarbon (perfluorooctylbromide, PFOB, which remains in a liquid

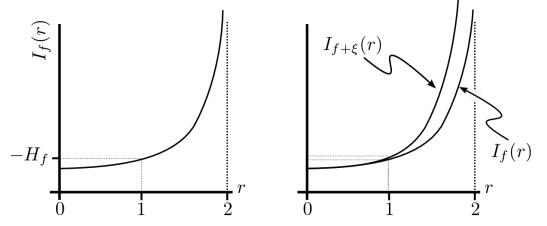


FIG. 2. Left panel: A plot of $I_f(r)$ (left) showing that $I_f(1) = -H_f$ and that $I_f(r)$ grows without bound as $r \rightarrow 2$. Right panel: Even though two similar waveforms $f(t)$ and $f(t)+\xi(t)$ may have nearly equal entropies, H_f , it is possible that as $r \rightarrow 2$ their Renyi entropies may diverge.

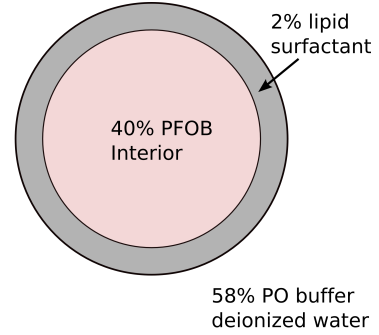


FIG. 3. A cross-sectional diagram of the nanoparticles used in our study.

state at body temperature and at the acoustic pressures used in this study⁸) emulsions encapsulated by a lipid-surfactant monolayer.^{9,10} The nominal sizes for each formulation were measured with a submicron particle analyzer (Malvern Zetasizer, Malvern Instruments). Particle diameter was measured at $200 \pm 30 nm$.

B. Animal model

The study was performed according to an approved animal protocol and in compliance with guidelines of the Washington University institutional animal care and use committee.

The model used is the transgenic K14-HPV16 mouse in which the ears typically exhibit squamous metaplasia, a pre-cancerous condition, associated with abundant neovascularity that expresses the $\alpha_v\beta_3$ integrin. Eight of these transgenic mice^{11,12} were treated with 1.0 mg/kg i.v. of either $\alpha_v\beta_3$ -targeted nanoparticles (n=4) or untargeted nanoparticles (n=4) and imaged dynamically for one hour using a research ultrasound imager (Vevo 660 30MHz probe) modified to store digitized RF waveforms acquired at 0, 15, 30, and 60 minute time points. In both targeted and untargeted cases, the mouse was placed on a

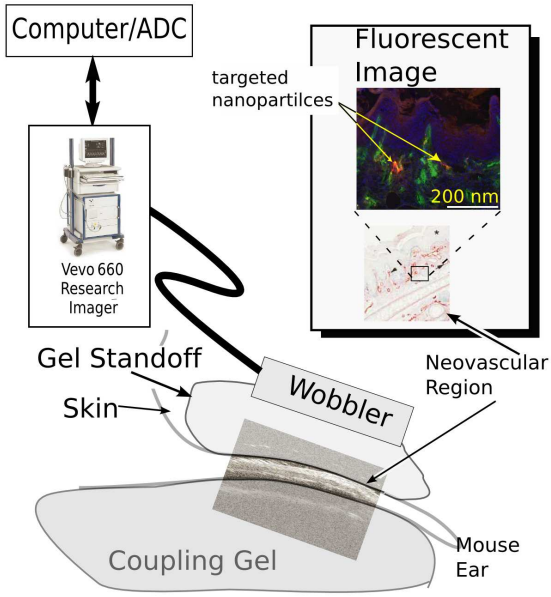


FIG. 4. A diagram of the apparatus used to acquire RF data backscattered from HPV mouse ears *in vivo* together with an histologically stained section of the ear indicating portions where $\alpha_v\beta_3$ -targeted nanoparticles could adhere and a fluorescent image demonstrating presence of targeted nanoparticles.

heated platform maintained at 37°C , and anesthesia was administered continuously with isoflurane gas (0.5%).

C. Ultrasonic Data Acquisition

A diagram of our apparatus is shown in Figure (4). Radio frequency data were acquired with a research ultrasound system (Vevo 660, Visualsonics, Toronto, Canada), with an analog port and a sync port to permit digitization. The tumor was imaged with a 40 MHz single element “wobbler” probe and the RF data corresponding to single frames were stored on a hard disk for later off-line analysis. The frames (acquired at a rate of 30 Hz) consisted of 384 lines of 4096 eight-bit words acquired at a sampling rate of 500 MHz using a Gage CS82G digitizer card (connected to the analog-out and sync ports of the Vevo) in a controller PC. Each frame corresponds spatially to a region 0.8 cm wide and 0.3 cm deep.

The wobbler transducer used in this study is highly focused (3mm in diameter) with a focal length of 6 mm and a theoretical spot size of $80 \times 1100 \mu\text{m}$ (lateral beam width \times depth of field at -6dB), so that the imager is most sensitive to changes occurring in the region swept out by the focal zone as the transducer is “wobbled”. Accordingly, a gel standoff was used, as shown in Figure (4), so that this region would contain the mouse ear.

A close-up view showing the placement of transducer,

gel standoff, and mouse ear is shown in the bottom of the figure. Superposed on the diagram is a B-mode gray scale image (*i.e.* logarithm of the analytic signal magnitude). Labels indicate the location of skin (top of ear insert), the structural cartilage in the middle of the ear, and a short distance below this, the echo from the skin at the bottom of the ear. Directly above this is an image of a histological specimen extracted from a HPV mouse model that has been magnified 20 times to permit better assessment of the thickness and architecture of the sites where $\alpha_v\beta_3$ targeted nanoparticle might attach (red by β_3 staining). Skin and tumor are both visible in the image. On either side of the cartilage (center band in image), extending to the dermal-epidermal junction, is the stroma. It is filled with neoangiogenic microvessels. These microvessels are also decorated with $\alpha_v\beta_3$ nanoparticles as indicated by the fluorescent image (labeled, in the upper right of the figure) of a bisected ear from an $\alpha_v\beta_3$ -injected K14-HPV16 transgenic mouse (Neumann, *et al.*, manuscript in preparation). It is in this region that the $\alpha_v\beta_3$ -targeted nanoparticles are expected to accumulate, as indicated by the presence of red β_3 stain in the magnified image of a histological specimen also shown in the image.

D. Ultrasonic Data Processing

Each of the 384 RF lines in the data was first up-sampled from 4096 to 8192 points, using a cubic spline fit to the original data set in order to improve the stability of the thermodynamic receiver algorithms. Previous work has shown benefit from increased input waveform length.^{13,14} Next, a moving window analysis was performed on the upsampled data set using a rectangular window that was advanced in $0.064 \mu\text{s}$ steps (64 points), resulting in 121 window positions within the original data set. This was done using both continuous entropy, H_f and Renyi entropy $I_f(1.99)$ analysis of the RF segments within each window in order to produce an image (either H_f or $I_f(1.99)$) for each time point in the experiment. As described previously, the density function, $w_f(y)$ used to compute H_f and $I_f(r)$ is computed using a Fourier series representation.¹⁵ For this study, where the desire was to compute $I_f(r)$ as near to its singular value as possible, it was found that 16384 terms were required for accurate estimation. In order to complete computations in a reasonable amount of time all calculations were performed on a linux cluster using Open MPI.

E. Image Processing

All RF data were processed off-line to reconstruct images using information theoretic, either H_f or $I_f(1.99)$. Subsequently, a histogram of pixel values for the composite of the 0, 15, 30, and 60 minute images was computed, either H_f or $I_f(1.99)$. Image segmentation of each type

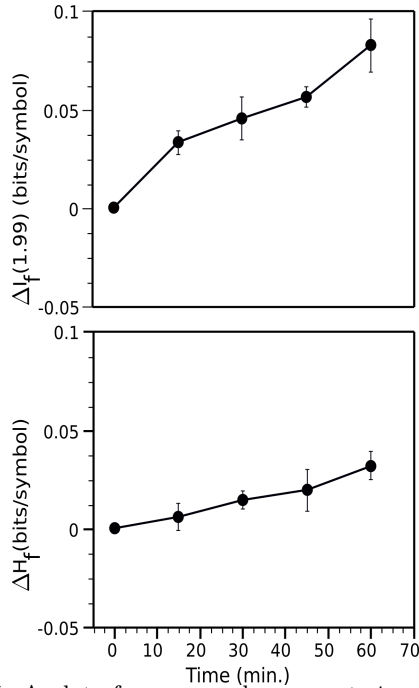


FIG. 5. A plot of average enhancement, *i.e.*, change relative to value at time 0, obtained by analysis of $I_f(1.99)$ (top) and H_f (bottom) images from four HPV mice injected with $\alpha_v\beta_3$ targeted nanoparticles.

of image, either H_f or $I_f(1.99)$, at each time point in the experiment was then performed automatically using its corresponding histogram according to the following threshold criterion: the lowest 7 % of pixel values were classified as “targeted” tissue, while the remaining were classified as “untargeted” (histogram analysis was also performed using 10 and 13 percent thresholds, with 7 percent having the best statistical separation between time points). The mean value of pixels classified as “targeted” was computed at each time post-injection.

IV. RESULTS AND DISCUSSION

The results obtained after injection of targeted nanoparticles, by either the $I_f(1.99)$ or H_f receivers, are shown in the top and bottom panels of Figure (5). Both panels compare the growth, with time, of the change (relative to 0 minutes) in mean value of receiver output in the enhanced regions of images obtained from all four of the animals in the targeted group. Standard error bars are shown with each point. At fifteen minutes the change in mean value if $I_f(1.99)$ is more than two standard errors from zero, implying statistical significance at the 95% level. As the bottom panel shows it is 30 minutes before H_f is more than twice the standard error from zero.

The results obtained after injection of nontargeted nanoparticles, by either the $I_f(1.99)$ or H_f receivers are shown, in the top and bottom panels of Figure (6). Nei-

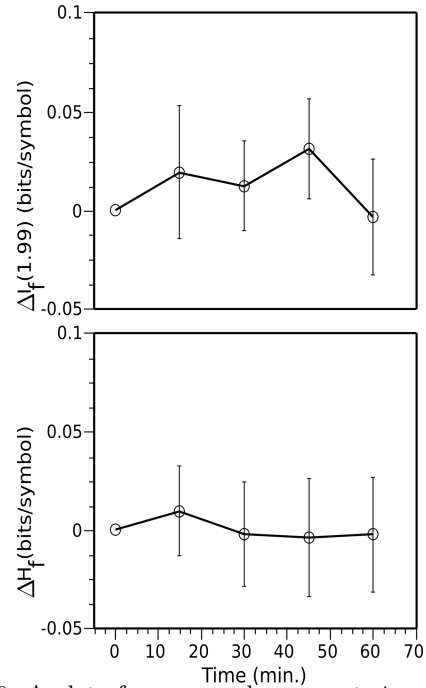


FIG. 6. A plot of average enhancement, *i.e.*, change relative to value at time 0, obtained by analysis of $I_f(1.99)$ (top) and H_f (bottom) images from four HPV mice injected with non targeted nanoparticles. Neither plot exhibits a statistically significant change.

ther receiver exhibits a statistically significant change in output over the course of the experiment.

The value of 1.99 was chosen after an initial round of numerical experimentation to assess numerical stability of receiver output (while also varying the number of terms required for the Fourier series reconstruction of $w_f(y)$) versus computation time. As the goal is ultimately to develop an algorithm of clinical utility, the execution time of one week required to compute the $I_f(1.99)$ images for this study was taken as an upper acceptable bound. Comparison of the data in Figures (5) and (6) show that $I_f(1.99)$ is able to detect accumulation of targeted nanoparticles in only half the time (post-injection) required by H_f . Pharmacokinetic dynamics would lead us to expect the steady increase of targeted nanoparticles in the region ofinsonification post-injection. Both plots of Figure (5) are consistent with this model, however, we may conclude that $I_f(1.99)$ is more sensitive to their presence than H_f . Future studies will concentrate on increasing the computational efficiency of our algorithm so that the region closer to $r = 2$ may be explored.

Acknowledgments

This study was funded by NIH EB002168, HL042950, and CO-27031 and NSF DMS 0501079. The research was carried out at the Washington University Department of

- ¹ M. S. Hughes, J. N. a. A. J. M. McCarthy, J. E.; Marsh, R. G. Neumann, R. W. Fuhrhop, K. D. Wallace, D. R. Znidersic, B. N. Maurizi, S. L. Baldwin, G. M. Lanza, and S. A. Wickline, "Properties of an entropy-based signal receiver with an application to ultrasonic molecular imaging", *Journal of the Acoustical Society of America* **121**, 3542–3557 (2007).
- ² R. S. Bucy and P. D. Joseph, *Filtering for Stochastic Processes with Applications to Guidance* (Chelsea Publishing Company, New York, NY) (1987).
- ³ N. Wiener, *Extrapolation, interpolation, and smoothing of stationary time series : with engineering applications* (M.I.T. Press, Cambridge, MA) (1949).
- ⁴ U. Grenander and M. Rosenblatt, *Statistical Analysis of Stationary Time Series* (Chelsea Publishing Company, New York, NY) (1984).
- ⁵ R. N. Bracewell.
- ⁶ T. M. Cover and J. A. Thomas, *Elements of Information Theory* (wiley-Interscience, New York) (1991).
- ⁷ R. Tolman, *The Principles of Stastical Mechanics* (Dover Press, New York, NY) (1979).
- ⁸ M. S. Hughes, J. N. Marsh, J. Arbeit, R. Neumann, R. W. Fuhrhop, G. M. Lanza, and S. A. Wickline, "Ultrasonic molecular imaging of primordial angiogenic vessels in rabbit and mouse models with $\alpha_v\beta_3$ -integrin targeted nanoparticles using information-theoretic signal detection: Results at high frequency and in the clinical diagnostic frequency range", *Proceedings of the 2005 I.E.E.E. Ultrasonics Symposium* (2005).
- ⁹ S. Flacke, S. Fischer, M. J. Scott, R. J. Fuhrhop, J. S. Allen, M. McLean, P. Winter, G. A. Sicard, P. J. Gaffney, S. A. Wickline, and G. M. Lanza, "Novel mri contrast agent for molecular imaging of fibrin implications for detecting vulnerable plaques", *Circulation* **104**, 1280–1285 (2001).
- ¹⁰ G. M. Lanza, K. D. Wallace, M. J. Scott, W. P. Cacheris, D. R. Abendschein, D. H. Christy, A. M. Sharkey, J. G. Miller, P. J. Gaffney, and S. A. Wickline, "A novel site-targeted ultrasonic contrast agent with broad biomedical application", *Circulation* **94**, 3334–3340 (1996).
- ¹¹ J. M. Arbeit, R. R. Riley, B. Huey, C. Porter, G. Kelloff, R. Lubet, J. M. Ward, and D. Pinkel, "chemoprevention of epidermal carcinogenesis in k14-hpv16 transgenic mice", *Cancer Research* **59**, 3610–3620 (1999).
- ¹² J. M. Arbeit, K. Mnger, P. M. Howley, and D. Hanahan, "Progressive squamous epithelial neoplasia in k14-human papillomavirus type 16 transgenic mice", *Journal of Virology* **68**, 4358–4368 (1994).
- ¹³ M. Hughes, "Analysis of digitized waveforms using shannon entropy", *Journal of the Acoustical Society of America* **93**, 892–906 (1993).
- ¹⁴ M. Hughes, "Analysis of digitized waveforms using shannon entropy. ii. high-speed algorithms based on green's functions", *Journal of the Acoustical Society of America* **95**, 2582–2588 (1994).
- ¹⁵ M. Hughes, "Analysis of ultrasonic waveforms using shannon entropy", *Proceedings of the 1992 I.E.E.E. Ultrasonics Symposium* **2**, 1205–1209 (1992).